

# **An assessment of structural enthalpy and crystallization pathways of $\text{Mg}_{65}\text{Zn}_{30}\text{Ca}_5$ bulk metallic glass and amorphous films**

**Scott Gleason, David Miskovic, Nicholas Hamilton, Kevin Laws, Michael Ferry**

UNSW Australia  
School of Material Science and Engineering

August 8, 2017

# ABSTRACT

The structural nature and thermal stability of amorphous alloys is highly dependent on the method by which they are produced, i.e. their relaxation rate upon cooling. Both bulk samples and metallic glass films of  $\text{Mg}_{65}\text{Zn}_{30}\text{Ca}_5$  were produced by copper mold casting and direct current (DC) magnetron sputtering onto aluminium substrates, respectively. Comparisons between structural enthalpy, crystallization pathways, relaxation and crystallization kinetics of the bulk samples and films were examined by elevated temperature XRD and DSC. Compared with equivalent experiments on the bulk alloy, results for the thin films show distinct differences in structural enthalpy and deviations from the expected crystalline phase evolution, displaying minor peak shifts, failure of some phases to evolve, and variations in the evolution rates.

# TABLE OF CONTENTS

<b>ABSTRACT</b>	<b>i</b>
<b>TABLE OF CONTENTS</b>	<b>1</b>
<b>1 INTRODUCTION</b>	<b>1</b>
<b>2 METHOD</b>	<b>1</b>
2.1 Master alloy . . . . .	1
2.2 DC magnetron sputtering . . . . .	1
2.3 Stylus profiler analysis . . . . .	2
2.4 EDS analysis . . . . .	2
2.5 DSC characterization . . . . .	2
2.6 XRD characterization . . . . .	2
<b>3 RESULTS</b>	<b>3</b>
3.1 Alloy composition . . . . .	3
3.2 DSC . . . . .	3
3.2.1 Isochronic DSC . . . . .	3
3.2.2 Fragility . . . . .	4
3.3 DSC deconvolution . . . . .	5
3.3.1 Onset determination . . . . .	5
3.3.2 Reaction enthalpy . . . . .	5
3.3.3 Relaxation enthalpy . . . . .	6
3.4 XRD . . . . .	6
3.4.1 Annealing XRD . . . . .	6
3.4.2 Dynamic XRD . . . . .	6
<b>4 DISCUSSION</b>	<b>6</b>
<b>5 CONCLUSIONS</b>	<b>7</b>
<b>6 ACKNOWLEDGEMENTS</b>	<b>7</b>
<b>7 REFERENCES</b>	<b>7</b>

# 1 INTRODUCTION

The structural nature and thermal stability of amorphous alloys is highly dependent on the method by which they are produced, i.e. their relaxation rate upon cooling. Both bulk samples and metallic glass films of  $\text{Mg}_{65}\text{Zn}_{30}\text{Ca}_5$  were produced by copper mold casting and direct current (DC) magnetron sputtering onto aluminium substrates, respectively. Comparisons between structural enthalpy, crystallization pathways, relaxation and crystallization kinetics of the bulk samples and films were examined by elevated temperature XRD and DSC. Compared with equivalent experiments on the bulk alloy, results for the thin films show distinct differences in structural enthalpy and deviations from the expected crystalline phase evolution, displaying minor peak shifts, failure of some phases to evolve, and variations in the evolution rates.

## 2 METHOD

### 2.1 Master alloy

The master alloy of  $\text{Mg}_{65}\text{Zn}_{30}\text{Ca}_5$  was produced using high-purity elements of Mg (99.85 wt%), Zn (99.995 wt%), and Ca (99.8 wt%). The alloy was prepared by induction melting in boron nitride coated graphite crucibles, purged with Ar (99.997 vol.% purity) five times, and protected with a circulating Ar atmosphere. Alloy homogeneity was ensured by heating and cooling through a cycle of 700°C, 385°C, 650°C, 385°C, 650°C to a casting temperature of 500 °C and 450°C for injection and gravity casting respectively. Bulk amorphous  $\text{Mg}_{65}\text{Zn}_{30}\text{Ca}_5$  rods of 2.5mm diameter and plates of thickness of  $XX\mu\text{m}$  were produced by copper mold injection casting. The 25.4mm diameter targets were prepared from a cylindrical copper mold gravity castings sectioned to thicknesses of 3.25mm. All samples and targets were stored under Ar when not being examined or used.

### 2.2 DC magnetron sputtering

Films were produced from an in-house DC magnetron sputtering facility with Ar working gas (99.997 vol.% purity). The power was 15W, typical voltage of 290 – 350V, nominal chamber pressure of 1 bar, substrate temperature of 25°C, and Ar flow of 3.01 SCCM. Films were deposited directly onto to Al DSC lid substrates. Depositions were for a period of 35 minutes. Deposition rate was estimated at 1.2nm/s.

## 2.3 Stylus profiler analysis

Nominal film thickness was measured by a stylus profiler (Dektak 2A, Bruker, Germany). A glass slide was placed under the substrates within the sputtering chamber, allowing the substrates to act as a mask. Profile measurements were taken by measuring the height difference between the bare glass and the film coated glass. This film thickness was used to estimate the sputter deposition rate.

## 2.4 EDS analysis

Alloy composition and homogeneity were confirmed by SEM-EDS (S3400, Hitachi, Japan). Hyper-maps were collected with an accelerating voltage of 15 – 20 kV, and a probe current of 50  $\mu$ A. (Conditions; counts were 5000 kps or better, dead time was less than 20 %, and working distance was 10 mm).

## 2.5 DSC characterization

Isochronic DSC (204 F1 Phoenix, Netzsch, Selb, Germany) was carried out in Al crucibles under a protective Ar atmosphere (99.997 vol.% purity). Scans were performed at heating rates ( $\beta$ s) of 5 to 100 K/min.

Isothermal relaxation DSC was performed by heating samples at 20 K/min to the desired annealing temperature, holding for desired time, and Ar quenching to room temperature.

For annealed XRD the samples were heat treated in the DSC by heating to the desired temperature at 20 K/min followed by Ar quenching to room temperature.

## 2.6 XRD characterization

Annealing XRD (Empyrean, PANalytical, Cu  $K_{\alpha}$  X-ray source,  $\lambda = 1.541 \text{ \AA}$ ) was performed at room temperature. (Generator Voltage 45, Tube Current 40, Scan Step Size 0.0262606, Time per Step 397.29).

Dynamic XRD (D8, Bruker, Cu  $K_{\alpha}$  X-ray source,  $\lambda = 1.541 \text{ \AA}$ ) was performed by raising temperature at a rate of 20 K/min and performing scans *in situ*. The first scan was performed at 35°C, then 75°C, after which temperature was raised in 5 K increments until reaching the peak temperature at 185°C. The  $2\theta$  scans from 31 – 60° were completed within 1092 sec.

(18min, 12sec) to minimise the effects of recrystallisation during the experiment. (Generator Voltage 45, Tube Current 100, Scan Step Size 0.02, Time per Step 134.4).

### 3 RESULTS

#### 3.1 Alloy composition

From the 35 minute depositions a nominal film thickness of  $2.5\mu m$  was obtained, giving a deposition rate of approximately  $1.2nm/s$ . The temperature within the chamber was found to rise  $3 - 4^{\circ}C$ , significantly less than the expected  $20K$  suggested by similar setups [1].

EDS analysis shows good agreement in the nominal composition for both the bulk and film  $Mg_{65}Zn_{30}Ca_5$ , see Table 1.

EDS Analysis	Bulk (at%)	Film (at%)
Mg	$64.85 \pm 3.18$	$62.92 \pm 3.24$
Zn	$29.55 \pm 0.82$	$31.17 \pm 0.95$
Ca	$5.60 \pm 0.17$	$5.91 \pm 0.19$

Table 1: EDS composition of bulk and film  $Mg_{65}Zn_{30}Ca_5$  in atomic weight percent.

#### 3.2 DSC

##### 3.2.1 Isochronic DSC

Isochronic DSC was performed on the bulk and film  $Mg_{65}Zn_{30}Ca_5$  to examine the thermal properties. The bulk alloy was relaxed at  $120^{\circ}C$  for 10 minutes before DSC measurements to ensure the  $T_g$  was clearly visible. The film was not relaxed as unlike the bulk the loss in free volume from relaxation would be significant and make differences between the samples much more difficult to observe [source needed???].

The bulk  $Mg_{65}Zn_{30}Ca_5$  was examined at heating rates ( $\beta$ s) of 5, 10, 15, 20, 30, 40, 60, 80, and  $100 K/min$  to observe changes in the  $T_g$  and the  $T_x$ s with  $\beta$ . As expected greater  $\beta$  resulted in greater signal strength, exothermic peaks shifting to higher start temperatures, and an increase in thermal lag resulting in later exothermic finish temperatures and curve convolution. With this convolution the  $T_g$  and  $T_{x1}$  remained clearly visible for all  $\beta$ s, but  $T_{x2,4,5}$  were only visible at low  $\beta$ s, and  $T_{x3}$  was not clear at any  $\beta$ , see Figure 1.

The film was examined at  $\beta$ s of 15, 20, 30, 40, 60, 80, and 100 K/min. The lower  $\beta$ s of 5 and 10 K/min were not utilised owing to the lower film signal compared to the bulk. The reduced signal was likely from the low mass of the film, about  $\frac{1}{10}$  that of the bulk. The film showed the expected variable relationships with increasing  $\beta$  as observed in the bulk. The signal intensity increased at a compatible rate to bulk up until  $\beta$ s of 80 and 100 K/min. These final two  $\beta$ s showed great increases in the signal intensity. The exothermic peaks all convoluted together making many of the thermodynamic events difficult to observe. It also appeared that all exothermic events shifted to lower temperatures as compared to the bulk. The  $T_g$  and  $T_{x1}$ s were less defined than for the bulk, but could still be identified for all  $\beta$ s. For all  $\beta$ s the  $T_{x2-5}$  onsets could not be easily identified, see Figure 2. fig:DSC\_vHeatingRate\_Film

### 3.2.2 Fragility

Using the isochronic DSC data the fragility ( $m$ ) of the  $\text{Mg}_{65}\text{Zn}_{30}\text{Ca}_5$  system could be established for both the bulk and film. Numerical solutions were used to fit the DSC variant of the Vogel–Fulcher–Tammann (VFT) relationship for  $\beta$  [2]. Busch1998

$$\beta^{-1} = \tau_0 e^{\left(\frac{D^* T_0}{T_g - T_0}\right)} \quad (1) \quad \text{equ:VFT}$$

Where  $\tau_0$  is a pre-exponential factor,  $D^*$  is the liquid fragility parameter, and  $T_0$  is the VFT temperature where the barrier to flow becomes infinite.

The  $m$  could then be calculated from Equation 2 [3, 4]. edding2002, Wei2014

$$D^* = 590 / (m - 16) \quad (2) \quad \text{equ:dSta}$$

Using these two equations for the bulk it was found  $\beta^{-1} = 1.338E - 16 e^{5274\left(\frac{1}{T-T_0}\right)}$  with an Adj.  $R^2 = 0.972$ . This gave a  $D^* = 20.4$ , and a  $m = 44.9$ . The film was fitted to  $\beta^{-1} = 5.921E - 11 e^{2766\left(\frac{1}{T-T_0}\right)}$  with a lower confidence of Adj.  $R^2 = 0.861$ , likely owing to the reduced number of data points. This gave a  $D^* = 10.0$ , and  $m = 75.0$ , see Figure 3. fig:Fragility\_BulkFilm\_mValue

### 3.3 DSC deconvolution

#### 3.3.1 Onset determination

Numerical solutions were used to deconvolute the isochronic DSC data so the various  $T_x$  onsets could be accurately determined. This numerical fitting utilised a summation of skewed Gaussian curves to fit a target curve corresponding to the original data; as is a common method [5–9]. This fitting summation takes the form of Equation 3.

$$f(x) = \sum_{n=i}^n h_i e^{-\left(\frac{(x - T_i)^2}{(2c_j)^2}\right)} \quad (3)$$

Where  $h$  is the enthalpy peak intensity,  $T$  is the temperature at the enthalpy peak centre, and  $c$  is the Gaussian RMS width.

The final converged solutions of this fitting for both the bulk and film are shown in Figures 4 and 5 respectively. These results are tabulated in Table 2 for the bulk and Table 3 for the film. Note  $T_g$  and  $T_{x1}$  are obtained from the original raw data, not the deconvolution.

Heating Rate $\beta$ K/min	$T_g$	$T_{x1}$	$T_{x2}$	$T_{x3}$	$T_{x4}$	$T_{x5}$
100	136.1	164.8	193.4	201.8	240.2	262.4
80	132.0	160.0	194.4	201.9	238.2	260.3
60	129.6	157.7	190.0	197.8	232.9	259.0
40	126.6	155.2	189.0	200.0	226.4	254.7
30	126.2	151.5	187.0	198.4	221.0	251.1
20	125.1	149.8	188.4	197.0	216.0	246.8
15	123.8	148.3	186.2	195.6	212.2	243.9
10	123.5	144.5	183.4	192.9	207.4	239.8
5	120.5	141.1	179.7	187.5	199.8	232.7

Table 2: Bulk  $\text{Mg}_{65}\text{Zn}_{30}\text{Ca}_5$  alloy onset temperatures for the various DSC heating rates  $\beta$ . All temperatures are in  $^{\circ}\text{C}$ .

#### 3.3.2 Reaction enthalpy

The deconvolution fits were integrated to find the area under each curves. This information provides the specific enthalpy ( $h$ ) of the crystallization of each phase. This is presented in Tables 4 and 5 for the bulk and film respectively. Figure 8 shows the  $T_x$  onsets and specific enthalpy ( $h$ ) for both the bulk and film plotted together.



Heating Rate $\beta$ $K/min$	$T_g$	$T_{x1}$	$T_{x2}$	$T_{x3}$	$T_{x4}$	$T_{x5}$
100	108.5	128.6		177.3		240.3
80	106.0	121.2		165.6		238.8
60	107.3	134.0		176.1		237.8
40	100.2	119.8		170.7		234.2
30	95.3	110.4		169.5		232.5
20	95.5	115.2		170.5		229.4
15	92.5	113.5		168.8		224.0

Table 3: Film  $Mg_{65}Zn_{30}Ca_5$  alloy onset temperatures for the various DSC heating rates  $\beta$ . All temperatures are in  $^{\circ}C$ .

Heating Rate $\beta$ $K/min$	$h_{T_{x1}}$ $J/g$	$h_{T_{x2}}$ $J/g$	$h_{T_{x3}}$ $J/g$	$h_{T_{x4}}$ $J/g$	$h_{T_{x5}}$ $J/g$
100	59.59	6.97	49.16	22.84	46.08
80	42.61	6.08	32.33	18.27	31.25
60	30.02	4.05	25.41	16.76	19.81
40	16.93	4.36	12.44	11.13	11.68
30	12.03	3.68	9.32	9.18	9.02
20	7.18	2.21	4.99	5.67	5.78
15	5.48	2.01	3.65	4.69	4.43
10	3.45	1.43	2.28	3.14	2.92
5	1.65	0.69	1.09	1.47	1.42

Table 4: Bulk  $Mg_{65}Zn_{30}Ca_5$  alloy  $h$  of crystallisation for  $T_{x1-5}$  for the various DSC heating rates  $\beta$ ;  $h$  is in  $J/g$ .

### 3.3.3 Relaxation enthalpy

## 3.4 XRD

### 3.4.1 Annealing XRD

Note: Key XRD sources for  $Mg_{65}Zn_{30}Ca_5$  crystallisation phase identification [10–12] [\[Zhang2013, Zhang2012, Zhan](#)

### 3.4.2 Dynamic XRD

## 4 DISCUSSION

The use of a 60K DSC heating rate compared to the more commonly used 20K rate [sources] shifts peaks for the bulk  $Mg_{65}Zn_{30}Ca_5$  alloy about 8 - 15 degrees higher. This higher heating

Heating Rate $\beta$ $K/min$	$h_{T_{x1}}$ $J/g$	$h_{T_{x2}}$ $J/g$	$h_{T_{x3}}$ $J/g$	$h_{T_{x4}}$ $J/g$	$h_{T_{x5}}$ $J/g$
100	48.24		49.85		43.38
80	43.27		53.56		36.18
60	15.5		8.78		22.4
40	16.22		9.13		16.27
30	13.72		7.16		11.81
20	6.16		2.3		7.45
15	6.99		3.66		6.57

Table 5: Film  $Mg_{65}Zn_{30}Ca_5$  alloy  $h$  of crystallisation for  $T_{x1-5}$  for the various DSC heating rates  $\beta$ ;  $h$  is in  $J/g$ .

rates were used because crystallization events for the films were difficult to differentiation at the lower heating rate. Films show little shift to high temperature peaks with increases heating rates, but large shifts with relaxation. Bulk show the opposite behaviour, larger peaks shifts with higher heating rates and little shift with relaxation.

## 5 CONCLUSIONS

## 6 ACKNOWLEDGEMENTS

Yu Wang for his assistance with XRD experimentation and Rietveld refinement.

## 7 REFERENCES

- [1] J. Q. Wang, N. Chen, P. Liu, Z. Wang, D. V. Louzguine-Luzgin, M. W. Chen, and J. H. Perepezko. The ultrastable kinetic behavior of an Au-based nanoglass. *Acta Materialia*, 79(0):30–36, 2014.
- [2] R. Busch, W. Liu, and W. L. Johnson. Thermodynamics and kinetics of the  $Mg_{65}Cu_{25}Y_{10}$  bulk metallic glass forming liquid. *Journal of Applied Physics*, 83(8):4134–4141, 1998.
- [3] C. A. Angell and S. Borick. Specific heats  $C_p$ ,  $C_v$ ,  $C_{conf}$  and energy landscapes of glassforming liquids. *Journal of Non-Crystalline Solids*, 307 - 310:393–406, 2002.
- [4] Shuai Wei, Zach Evenson, Isabella Gallino, and Ralf Busch. The impact of fragility on the calorimetric glass transition in bulk metallic glasses. *Intermetallics*, 55:138–144, 2014.

- hour2010 [5] Samir K. Ashour and Mahmood A. Abdel-hameed. Approximate skew normal distribution. *Journal of Advanced Research*, 1(4):341–350, 2010.
- moto2007 [6] Yuzo Yamamoto, Yuichi Inoue, Teruaki Onai, Chikashi Doshu, Hiroshi Takahashi, and Hiroki Uehara. Deconvolution analyses of differential scanning calorimetry profiles of  $\beta$ -crystallized polypropylenes with synchronized x-ray measurements. *Macromolecules*, 40(8):2745–2750, 2007.
- pink2008 [7] Charles H. Spink. *Differential Scanning Calorimetry*, volume Volume 84, pages 115–141. Academic Press, 2008.
- pink2015 [8] Charles H. Spink. The deconvolution of differential scanning calorimetry unfolding transitions. *Methods*, 76:78–86, 2015.
- ffer2005 [9] Balázs Schäffer, Béla Schäffer, and D. Lőrinczy. Decomposition of dsc curves of dairy products with gaussian functions. *Journal of Thermal Analysis and Calorimetry*, 82(2):531–535, 2005.
- hang2013 [10] Y. N. Zhang, G. J. Rocher, B. Briccoli, D. Kevorkov, X. B. Liu, Z. Altounian, and M. Medraj. Crystallization characteristics of the Mg-rich metallic glasses in the Ca-Mg-Zn system. *Journal of Alloys and Compounds*, 552:88–97, 2013.
- hang2012 [11] Yi-Nan Zhang, Dmytro Kevorkov, Xue Dong Liu, Florent Bridier, Patrice Chartrand, and Mamoun Medraj. Homogeneity range and crystal structure of the  $\text{Ca}_2\text{Mg}_5\text{Zn}_{13}$  compound. *Journal of Alloys and Compounds*, 523:75–82, 2012.
- hang2011 [12] Yi-Nan Zhang, Dmytro Kevorkov, Florent Bridier, and Mamoun Medraj. Experimental study of the Ca-Mg-Zn system using diffusion couples and key alloys. *Science and Technology of Advanced Materials*, 12(2):025003, 2011.
- Aji2013 [13] Daisman PB Aji, Akihiko Hirata, Fan Zhu, Liu Pan, K Madhav Reddy, Shuangxi Song, Yanhui Liu, Takeshi Fujita, Shinji Kohara, and Mingwei Chen. Ultrastrong and ultrastable metallic glass. *arXiv preprint arXiv:1306.1575*, 2013.

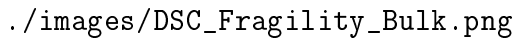
The figure is a plot showing the fragility of bulk Mg<sub>65</sub>Zn<sub>30</sub>Ca<sub>5</sub> alloy. It displays multiple DSC curves for different heating rates, stacked vertically. The x-axis represents temperature in degrees Celsius, and the y-axis represents heat flow. The curves show a glass transition region that shifts to higher temperatures as the heating rate increases. An inset in the top right corner provides a detailed view of the DSC curves for a heating rate of 100 K/min, with labels for the glass transition temperature (T<sub>g</sub>) and the crystallization exotherm (T<sub>x</sub>es).

Figure 1: Bulk Mg<sub>65</sub>Zn<sub>30</sub>Ca<sub>5</sub> relaxed at 120 °C for 10 minutes and heated at various heating rates. The insert stacks the differential scanning calorimetry (DSC) curves and labels the  $T_g$  and  $T_{xes}$  of the 100K/min sample.

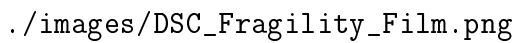
The figure is a plot showing the fragility of unrelaxed film Mg<sub>65</sub>Zn<sub>30</sub>Ca<sub>5</sub> alloy. It displays multiple DSC curves for different heating rates, stacked vertically. The x-axis represents temperature in degrees Celsius, and the y-axis represents heat flow. The curves show a glass transition region that shifts to higher temperatures as the heating rate increases. An inset in the top right corner provides a detailed view of the DSC curves for a heating rate of 100 K/min, with labels for the glass transition temperature (T<sub>g</sub>) and the crystallization exotherm (T<sub>x</sub>es).

Figure 2: Unrelaxed film Mg<sub>65</sub>Zn<sub>30</sub>Ca<sub>5</sub> heated at various heating rates. The insert stacks the DSC curves and labels the  $T_g$  and  $T_{xes}$  of the 100K/min sample.

./images/Bulk\_Film\_Fragility.png

Figure 3: Fitted fragility ( $m$ ) for the  $\text{Mg}_{65}\text{Zn}_{30}\text{Ca}_5$  system obtained by DSC at various heating rates

m\_mValue



Figure 4: DSC deconvolution for the bulk. From left to right, top to bottom, 5, 10, 15, 20, 30, 40, 60, 80, 100 K/min.

1k\_Decon



Figure 5: DSC deconvolution for the film. From left to right, top to bottom, 15, 20, 30, 40, 60, 80, 100 K/min.

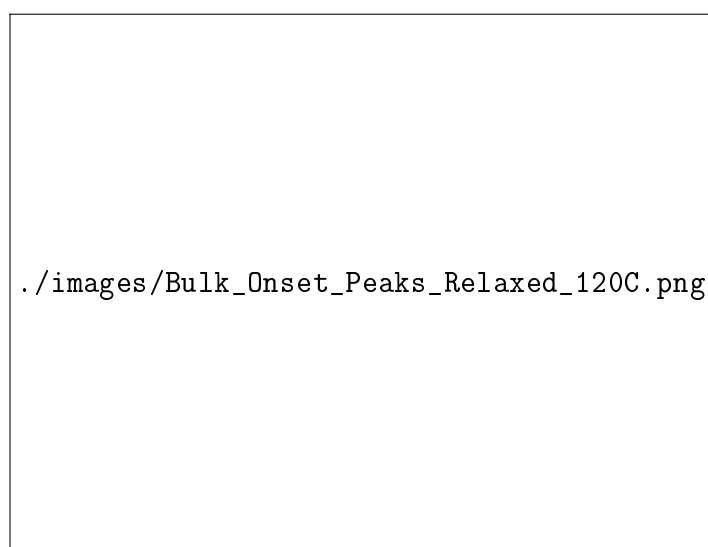


Figure 6: The  $T_g$ s and  $T_x$ es of the bulk  $Mg_{65}Zn_{30}Ca_5$  at all heating rates.

./images/Onsets\_BulkandFilm.png

Figure 7: The  $T_g$ s and  $T_x$ es of the bulk and film  $\text{Mg}_{65}\text{Zn}_{30}\text{Ca}_5$  at all heating rates.

./images/Decon\_Onsets\_BR.png

./images/Decon\_peak\_area\_BR.png

Figure 8: DSC onset temperatures and enthalpy of formation for the bulk and film.



./images/XRD\_Annealing\_Bulk.png

Figure 9: XRD pattern for Bulk  $\text{Mg}_{65}\text{Zn}_{30}\text{Ca}_5$  heated through several crystallization peaks identified from DSC

./images/XRD\_Annealing\_Film.png

Figure 10: XRD pattern for Film  $\text{Mg}_{65}\text{Zn}_{30}\text{Ca}_5$  heated through several crystallization peaks identified from DSC

./images/XRD\_Dynamic\_Bulk.png

(a)

./images/Bulk\_Heated\_XRD\_Waterfall3D\_Smooth2.png

(b)

Figure 11: (a) Stacked X-ray diffraction (XRD) patterns from the incremental heating of bulk  $\text{Mg}_{65}\text{Zn}_{30}\text{Ca}_5$ . (b) Cascading XRD patterns from the incremental heating of bulk  $\text{Mg}_{65}\text{Zn}_{30}\text{Ca}_5$ .

amic\_FullStack\_Film

./images/XRD\_Dynamic\_Film.png

(a)

amic\_WaterFall\_Film

./images/TF\_Facet\_HeatXRD\_Waterfall3D\_Smooth.png

(b)

mic\_Film

Figure 12: (a) Stacked XRD patterns from the incremental heating of film  $\text{Mg}_{65}\text{Zn}_{30}\text{Ca}_5$ . (b) Cascading XRD patterns from the incremental heating of film  $\text{Mg}_{65}\text{Zn}_{30}\text{Ca}_5$ .